energies

MDPI

Article

Assessment of Offshore Solar Photovoltaic and Wind Energy Resources in the Sea Area of China

Yanan Wu, Yang Bai, Qingwei Zhou and He Wu *

National Ocean Technology Center (NOTC), Tianjin 300112, China
* Correspondence: wh_crane@163.com

Abstract

Against the backdrop of China's "dual carbon" targets, the energy transition is accelerating. However, the expansion of onshore renewables is often constrained by land scarcity. Offshore areas thus present a promising alternative. In this study, high-resolution wind field data from 1995 to 2024 were generated using the WRF model driven by ERA5 reanalysis, enabling a 30-year spatiotemporal assessment of offshore wind power density (at 160 m hub height) and photovoltaic potential (PVP) across China's four major seas—the Bohai Sea, Yellow Sea, East China Sea, and South China Sea. The results show clear spatial and seasonal patterns: solar PV potential decreases from south to north, with the South China Sea exhibiting the highest and most stable annual average PVP (16–18%) and summer peaks exceeding 25%. Wind energy resources are spatially heterogeneous; the East China Sea and Taiwan Strait are identified as the richest zones, where wind power density frequently reaches 800–1800 W/m^2 during autumn and winter. Importantly, a pronounced seasonal complementarity is observed: wind peaks in autumn/winter while solar peaks in spring/summer at representative coastal sites. This study provides, for the first time, a long-term, integrated assessment of both offshore wind and solar resources over all four Chinese seas, offering quantitative data and a scientific basis for differentiated marine energy planning, optimized siting, and the design of wind–solar hybrid systems.

Keywords: offshore wind energy; photovoltaic power potential; spatiotemporal assessment; resource complementarity

1. Introduction

The global energy landscape is undergoing a profound transformation, shifting from traditional fossil fuels to renewable sources, driven by the urgent challenges of climate change and the overarching goal of achieving carbon neutrality [1]. In this transition, wind and solar energy have emerged as the most commercially viable and scalable clean energy technologies, playing a pivotal role in decarbonizing the power sector [2,3]. As the world's largest energy consumer and carbon emitter, China has committed to ambitious "Dual Carbon" goals: peaking carbon emissions before 2030 and achieving carbon neutrality by 2060 [4]. This commitment necessitates an unprecedented acceleration in the transition to a green and low-carbon energy structure. However, the extensive deployment of onshore wind and photovoltaic (PV) farms often encounters constraints such as limited land availability, ecological concerns, and potential conflicts with human settlements [5,6]. In this context, the vast maritime domain presents a promising alternative. China possesses an extensive coastline bordering the Bohai Sea, Yellow Sea, East China Sea, and South China Sea. These offshore regions are endowed with abundant wind and solar energy

Check for updates

Academic Editors: Brian D. Fath and Lars Johanning

Received: 14 November 2025
Revised: 18 December 2025
Accepted: 9 January 2026
Published: 16 January 2026

Copyright: © 2026 by the authors. Licensee MDPI, Basel, Switzerland. This article is an open access article distributed under the terms and conditions of the Creative Commons Attribution (CC BY) license.

resources [7]. The efficient development and utilization of these offshore renewable sources can not only alleviate the pressure on land resources but also provide proximate clean power to the economically developed coastal provinces, thereby enhancing energy security. This strategic utilization is considered a crucial component in realizing China's energy transition strategy [8–10].

Recent studies have progressively elucidated the significance and characteristics of China's offshore renewable resources. For instance, Li (2023) [11] identified an annual complementary relationship between offshore wind and solar resources in the South China Sea. Tian et al. (2023) [12] highlighted the highly uneven spatial distribution of China's onshore wind and solar technical potential, noting that over 76% is concentrated in Xinjiang and Inner Mongolia, while offshore wind potential is more evenly distributed among coastal provinces. Jiang (2023) [13] further underscored the immense and economically viable potential of combined offshore wind and solar (W-S) generation in China, estimating an annual potential of approximately 15,700 TWh, half of which could be achieved at a cost below €86/MWh—sufficient to meet coastal electricity demand. Additionally, Wang (2022) [14] summarized that wind-rich areas are mainly in western, northern, and coastal provinces, whereas solar-rich areas are predominantly in western and northern regions. Despite these valuable contributions, the existing body of research exhibits notable limitations. Most studies have focused on either a single energy type or a specific sea area, thereby lacking a systematic, integrated assessment and comparative analysis across all four major Chinese coastal seas—the Bohai Sea, Yellow Sea, East China Sea, and South China Sea [15–17]. Moreover, there is a scarcity of detailed, long-term (e.g., 30-year) climatological analyses that characterize the monthly spatiotemporal patterns of both wind and photovoltaic (PV) resources, particularly concerning their variation along the coasts of different provinces [18,19]. Such high-resolution, long-term assessments are crucial for understanding resource stability, seasonal variability, and for designing reliable hybrid energy systems [20,21].

To address these research gaps, this study conducts a comprehensive, long-term assessment of offshore wind energy (quantified by wind power density, E) and photovoltaic potential (PVP) across all four major Chinese seas. Utilizing high-resolution reanalysis data spanning over 30 years, our research specifically aims to:

(1) Reveal the monthly average spatial distribution patterns of wind and solar resources across the four sea areas over the past three decades.

(2) Select representative coastal points for each province to plot monthly time series of both resources, visually illustrating their interannual and seasonal variations and complementarity.

By providing a unified, long-term, and spatially explicit evaluation of both wind and solar resources across all key maritime zones, this study offers a foundational dataset and analytical framework to support differentiated marine energy planning, optimized project siting, and the design of integrated wind–solar hybrid systems.

2. Data and Methods

2.1. Data

2.1.1. Introduction to the WRF Model

This study utilizes the ERA5 reanalysis dataset to supply initial and boundary conditions for the WRF model, specifically employing its shortwave radiation, temperature data, and core wind fields for dynamical forcing. Compared to satellite products with higher spatial resolution, ERA5 offers irreplaceable comprehensive advantages for medium- to long-term climate simulations. As a global atmospheric reanalysis, it first provides a physically consistent and gap-free representation of the three-dimensional atmospheric state across extended periods (1995–2024), which is essential for generating a continuous,

high-temporal-resolution forcing dataset. Second, by assimilating vast amounts of historical observations, ERA5 delivers output variables—such as multi-level pressure, temperature, humidity, and wind fields—that maintain a high degree of spatiotemporal physical coherence. This multi-parameter consistency is crucial for the proper initialization and the dynamical-thermodynamic balance of complex models like WRF. Furthermore, its global coverage and standardized data structure ensure efficient compatibility with the WRF Preprocessing System (WPS). Although its native resolution of approximately 31 km is coarser than some alternatives, ERA5's outstanding performance in temporal coverage, data completeness, and multi-variable physical consistency makes it a reliable choice for constructing long-term, dynamically downscaled climate datasets, fully aligning with the objectives of this 30-year spatiotemporal resource assessment.

The wind field was generated using the WRF model. The Weather Research and Forecasting (WRF) model is a next-generation mesoscale numerical weather prediction system and data assimilation framework developed collaboratively by scientists from numerous U.S. research institutions and universities. The WRF model has two primary versions: the WRF-NMM, which is primarily used for real-time forecasting by U.S. operational weather prediction centers and is updated relatively slowly; and the WRF-ARW (Advanced Research WRF), which was selected for this project. The WRF-ARW version facilitates tight integration between operational forecasting and scientific research, is updated more frequently, and offers robust technical support services [22,23].

It utilizes a fully compressible, non-hydrostatic Euler equation set. The horizontal grid employs the Arakawa C-grid staggering, and the vertical coordinate uses a mass-based, terrain-following eta coordinate (Laprise, 1992), where the eta levels can be adjusted as needed. The model framework consists of a dynamics core governing atmospheric motions and physics schemes describing sub-grid scale processes. These physics schemes include:

Microphysics schemes: Describing water phase changes and cloud physical processes. Cumulus parameterization schemes: Accounting for the effects of sub-grid scale convective clouds. Land-surface models: Multi-layer schemes ranging from simple thermal diffusion to models considering the effects of snow cover and sea ice. Planetary boundary layer schemes: Utilizing methods like 2nd-order turbulence closure or non-local K-diffusion.

Radiation schemes: Comprising an atmospheric radiation model with multi-band longwave radiation and a simpler shortwave radiation scheme, considering clouds and surface properties.

The WRF model primarily consists of the following modules:

- Preprocessing System (WPS): This module is used to define the simulation domain, interpolate terrain data (this project used 10-mi2 min 2-min resolution data) onto the simulation grid, and interpolate meteorological data from other models (e.g., global models) to provide the initial background fields for the simulation.
- Data Assimilation (WRFDA): This optional module employs data assimilation techniques (this project used 3D-Var) to incorporate observational data from stations, satellites, radars, etc., to improve the initial and boundary conditions for the simulation.
- Main Numerical Integration Module (ARW): This component generates the initial background field and time-varying lateral boundary conditions, and performs the numerical integration of the governing equations.
- Post-processing Modules: These are used for analyzing and visualizing the model output (in NetCDF format).

Currently, the dynamic core and computational schemes of the WRF model are quite mature, offering significant advantages for simulating mesoscale weather phenomena.

Running the WRF model requires initial guess fields and time-varying boundary conditions provided by 3D atmospheric data from global models. Observational data

(e.g., from radiosondes and surface stations) is also assimilated to optimize the initial guess field and produce the final initial conditions for the model run. Furthermore, the influence of the ocean must be considered, requiring sea surface temperature data. For simulations involving typhoons, vortex initialization (e.g., specifying center location, central pressure) is necessary in the initial conditions.

The original NCAR-AFWA scheme within the WRF model employs a relatively simple function for representing the wind profile:

$$V_1(r) = \begin{cases} V_{max}\frac{r}{R_{max}} & r < R_{max} \\ V_{max}\left(\frac{r}{R_{max}}\right)^{\alpha} & r \geq R_{max} \end{cases} \quad (1)$$

Here, $V_{(r)}$ is the tangential wind speed, and r is the distance from the typhoon center. V_{max} and R_{max} represent the maximum wind speed and the radius of maximum wind, respectively, as provided in typhoon observation reports. The value of α is typically -0.5. Actual observations indicate that this formula yields satisfactory results near the typhoon center; however, it does not perform as well in representing the outer structural characteristics of the typhoon. To better account for the wind field structure in the typhoon's outer regions, the following wind profile form proposed by Chan and Williams (1987) can be considered [24]:

$$V_2(r) = V_{max}\frac{r}{R_{max}}exp\left\{\frac{1}{b}\left[1-\left(\frac{r}{R_{max}}\right)^{b}\right]\right\} \quad (2)$$

The parameter b in the equation above is to be determined. If the typhoon observation report includes information on the radius of 50-knot and 30-knot winds, the value of parameter b can be determined. Therefore, by building on the strengths of the two formulas mentioned above, a new wind profile is constructed:

$$V(r) = \begin{cases} V_1(r) & r < R_c \\ \frac{1}{2}(V_1(r)+V_2(r)) & r \geq R_c \end{cases} \quad (3)$$

where $V_{1(r)}$ and $V_{2(r)}$ represent the tangential wind speeds in Equations (1) and (2), respectively, and R_c is the distance from the typhoon center where $V_{1(r)} - V_{2(r)} = 0$.

2.1.2. WRF Model Configuration

This project utilized the WRF meteorological model for numerical simulation of wind fields. The background wind field was derived from ERA5 data, and the map projection employed was the Mercator projection. The time integration step was set to 120 s for the outer domain, with 37 vertical layers and a top-level pressure of 5000 Pa. The simulation period spanned 30 years, from 00:00 on 1 January 1995 to 23:00 on 31 December 2024. Based on relevant literature and preliminary simulation analyses of various schemes, the final selected physical parameterization schemes are presented in Table 1. The selection of physical parameterization schemes (Table 1) was guided by their proven performance in simulating East Asian monsoon climates and coastal wind fields over long-term periods, as documented in prior studies focusing on China's coastal regions. Specifically, the Lin microphysics scheme and the YSU planetary boundary layer scheme have been widely adopted and validated for regional climate downscaling and wind energy assessments over Chinese seas [25,26]. The Kain–Fritsch (new eta) cumulus scheme was chosen for its capability in handling convective processes in coastal and oceanic environments, a common feature in our study domain. This combination of schemes has demonstrated a good balance between computational efficiency and accuracy in reproducing the spatiotemporal

characteristics of surface and upper-level wind fields, as confirmed through our preliminary sensitivity experiments and validation against observations (Section 2.1.3). The simulation domain covered 105–125° E and 3–41° N.

Table 1. WRF Model Parameter Configuration.

Name	Configuration
Microphysics Scheme	Lin et al. Scheme
Cumulus Convection Scheme	Kain–Fritsch (new eta) Scheme
Longwave Radiation Scheme	RRTM Scheme
Shortwave Radiation Scheme	Dudhia Scheme
Planetary Boundary Layer Scheme	YSU Scheme
Surface Layer Scheme	Revised MM5 Monin-Obukhov Scheme
Land Surface Process Scheme	Unified Noah Land-Surface Model Scheme

2.1.3. WRF Model Validation

To validate the simulated wind field data generated by WRF, this study utilized measured data from observation stations for comparison. The locations and coordinates of these stations are shown in Figure 1. The validation was conducted using measured wind speed and direction data from stations P1 and P2 during the period of 7–15 November 2012, as well as their full-year data for 2022. Additionally, measured wind speed data from Buoy 1 and Buoy 2 from January 2020 to December 2020 and January 2021 to December 2021, along with data from the Sanshan Island temporary observation station in November 2024, were compared with the WRF-simulated data (Table 2). The results are presented in Figures 2–6. The figures indicate a good agreement between the measured and simulated wind speed and direction, demonstrating the reliability of the simulated data and supporting its use for subsequent calculations (Table 3).

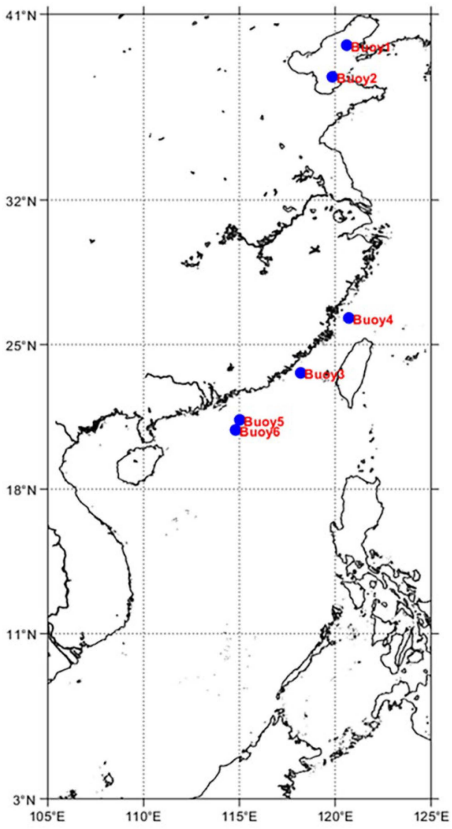


Figure 1. Location of Observation Points for Measured Data.

Table 2. Correlation coefficients between measured and simulated data.

r	Buoy1	Buoy2	Buoy5	Buoy6
Wind Speed	0.972	0.881	0.937	0.958
Wind Direction	0.942	0.934	0.887	0.963

Table 3. Error Analysis of Simulated vs. Measured Wind Speed (Unit: m/s).

Station	Parameter	MAE	RMSE
Buoy3	Wind Speed	1.40	1.89
Buoy4	Wind Speed	1.19	1.55

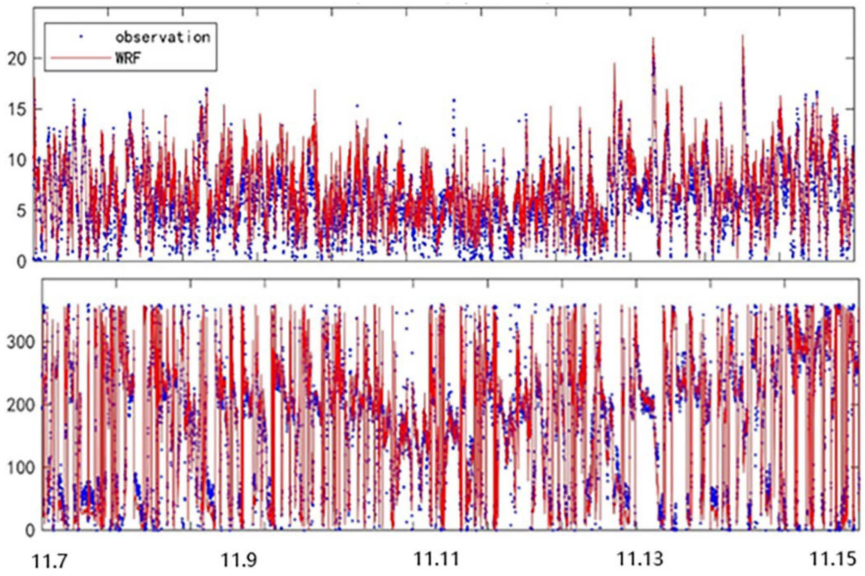


Figure 2. Comparison of Simulated and Measured Wind Speed and Wind Direction Data at Station Buoy1 for the Year 2022.

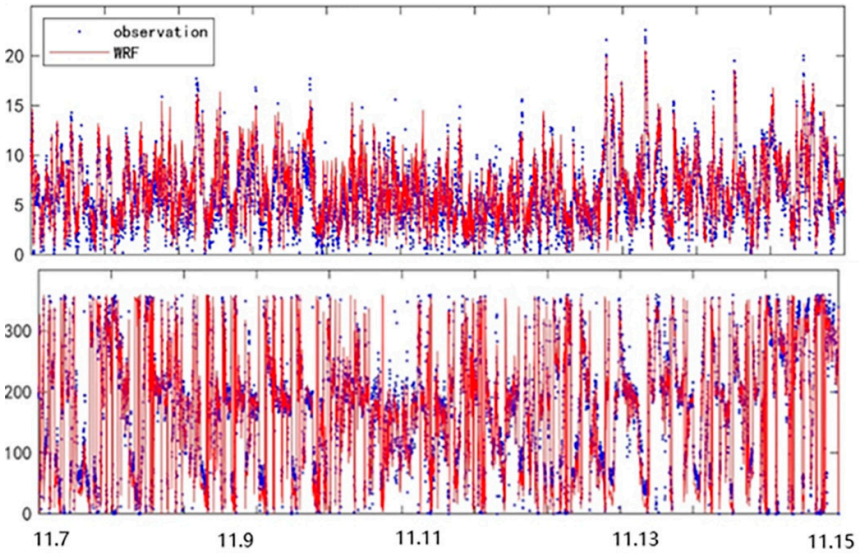


Figure 3. Comparison of Simulated and Measured Wind Speed and Wind Direction Data at Station Buoy2 for the Year 2022.

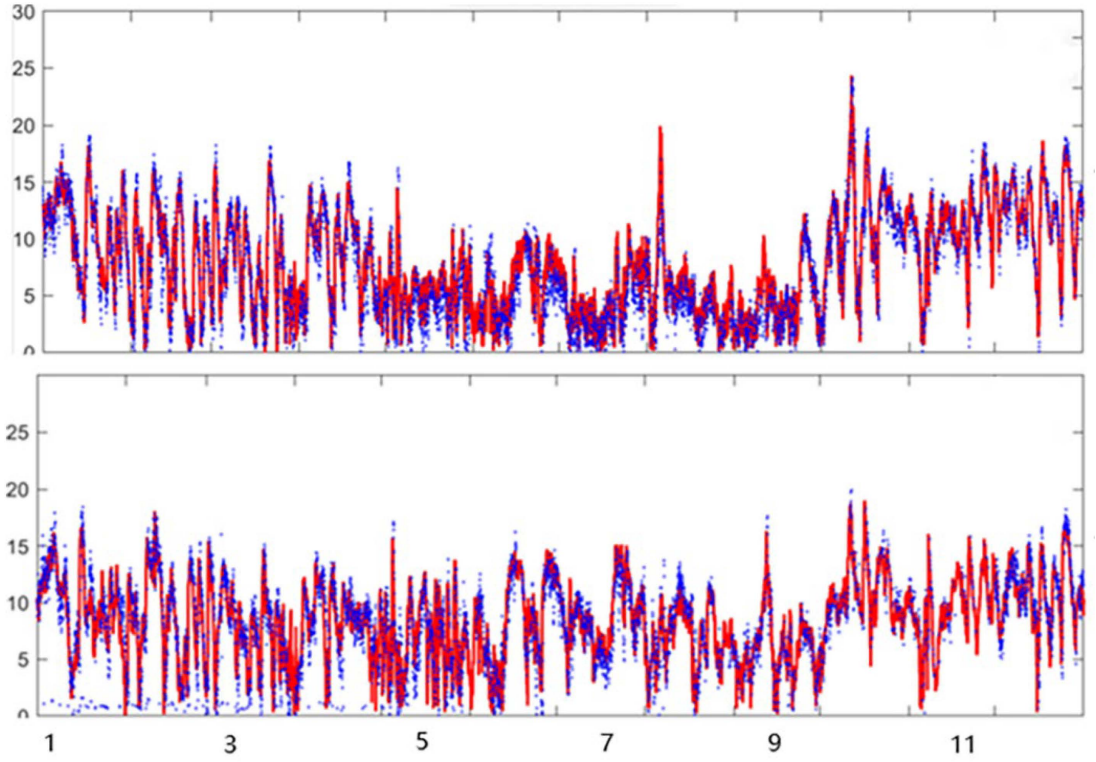


Figure 4. Comparison of Wind Speed at Buoy 3 and Buoy 4 from January to December 2021. Red represents simulations, blue represents measured data.

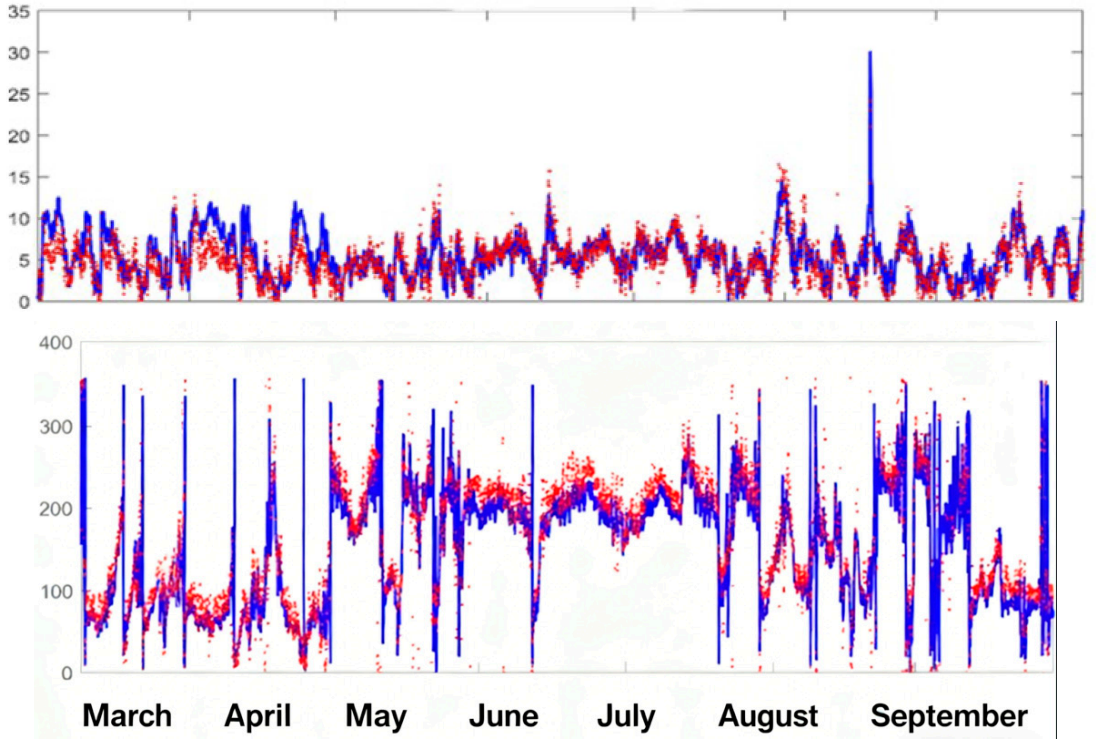


Figure 5. Comparison of Observed and Simulated Wind Speed and Direction Data at Buoy 5 from March to September 2020.

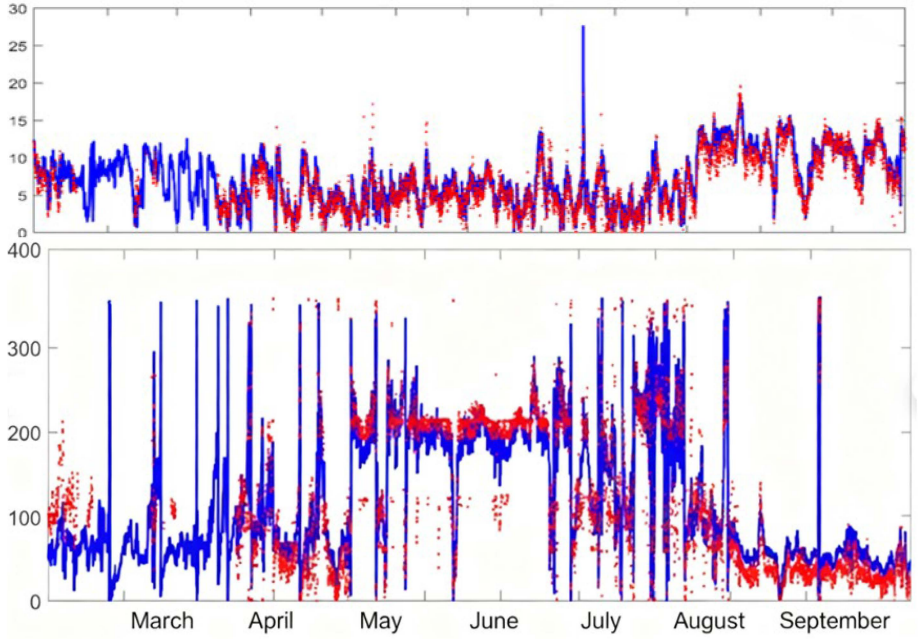


Figure 6. Comparison of Observed and Simulated Wind Speed and Direction Data at Buoy 6 from March to September 2020.

2.2. Photovoltaic Power Potential (PVP) Estimation

The Photovoltaic Power Potential (PVP) was estimated using the method proposed by Jerez et al. [27] and Mavromatakis et al. [28]. PVP is defined as the percentage of the output power of a photovoltaic (PV) module under actual environmental conditions relative to its output under Standard Test Conditions (STC). The specific expression is:

$$\mathrm{PVP}(t) = P_R(t)\,\frac{R(t)}{R_{STC}} \tag{4}$$

where R and R_{STC} are the shortwave radiation under actual environmental conditions and STC, respectively, with $R_{STC} = 1000\,\mathrm{W{\cdot}m^{-2}}$. P_R is the efficiency ratio, accounting for the efficiency change in the PV cell due to temperature variations, calculated as:

$$P_R(t) = 1 + \gamma[T_{cell}(t) - T_{STC}] \tag{5}$$

Here, T_{cell} is the cell temperature, $T_{STC} = 25\,^{\circ}\mathrm{C}$, and for monocrystalline silicon solar cells, the temperature coefficient is $\gamma = -0.005\,^{\circ}\mathrm{C}^{-1}$. Finally, considering the influence of air temperature (T), shortwave radiation (R), and wind speed (V) on the cell temperature, T_{cell} is calculated using the empirical formula [29]:

$$T_{cell}(t) = c_1 + c_2T(t) + c_3R(t) + c_4V(t) \tag{6}$$

The empirical coefficients are $c_1 = 4.3\,^{\circ}\mathrm{C}$, $c_2 = 0.943$, $c_3 = 0.028\,^{\circ}\mathrm{C}\cdot\mathrm{m}^2\cdot\mathrm{W}^{-1}$, and $c_4 = -1.528\,^{\circ}\mathrm{C}\cdot\mathrm{s}\cdot\mathrm{m}^{-1}$.

The photovoltaic output power will be lower than the rated power if T_{cell} exceeds 25 °C or if R falls below $1000\,\mathrm{W{\cdot}m^{-2}}$.

The empirical coefficients in Equation (6) were originally derived from land-based or laboratory studies under typical terrestrial conditions and have been widely adopted in photovoltaic performance modeling. However, their direct application to offshore environments entails certain uncertainties. Marine conditions—such as higher humidity, salt aerosol deposition, distinct diurnal temperature ranges, and typically stronger and more

consistent wind speeds—may alter the heat transfer dynamics at the PV module surface, potentially affecting the accuracy of the cell temperature estimation. In the absence of offshore-specific coefficients calibrated from measured PV performance data over Chinese seas, the use of these widely accepted empirical values provides a reasonable first-order approximation for large-scale and long-term assessments, as undertaken in this study. Nevertheless, the resulting PVP estimates should be interpreted with due consideration of these environmental differences. Future work incorporating in situ measurements or marine-adjusted coefficients would help reduce uncertainty and improve the precision of offshore photovoltaic potential evaluation.

The aforementioned methodology was selected for its direct applicability to our study's scale and data structure. It provides a clear, physics-based approach to estimate the key environmental impacts on PV performance using widely available meteorological inputs, which aligns well with the objectives and constraints of our current analysis.

2.3. Wind Power Parameter Calculation

2.3.1. Wind Power Density (WPD)

Comprehensive assessment of wind energy resources requires the consideration of multiple key indicators to fully reveal the potential and benefits of wind energy development in a region. This study systematically analyzes the wind power output intensity, reserve capacity, and technical-economic feasibility of the target area through three core indicators: Wind Power Density, total wind energy reserves, and technically exploitable potential. This integrated approach provides a holistic assessment of the wind energy resource distribution and development prospects in the study area.

Wind Power Density (WPD), defined as the utilizable wind power per unit area, is a crucial indicator for assessing wind energy resources. It directly influences the layout and performance optimization of wind turbines [30]. The mean WPD represents the wind energy passing through a unit area perpendicular to the wind direction per unit time [31]. The mean WPD (E) can be calculated statistically using the following formula:

$$E = \frac{1}{2}\rho V^3 \tag{7}$$

where E is the mean wind power density in W/m^2, ρ is the air density (assumed to be 1.225 kg/m^3 at standard sea level), and V is the wind speed at the specified height.

2.3.2. Wind Speed at Hub Height

Since ERA5 provides wind speed at 10 m, it is necessary to extrapolate it to the typical hub height of modern offshore wind turbines. The wind speed profile with height was modeled using the power law:

$$\frac{V_Z}{V_{10}} = \left(\frac{Z}{10}\right)^{\alpha} \tag{8}$$

where V_Z is the wind speed at the desired hub height z (assumed to be 160 m in this study), V_{10} is the wind speed at 10 m, and α is the wind shear exponent. Based on local meteorological tower data, the value of α was set to 0.11 for the coastal regions in this study [32].

2.3.3. Utilizable Wind Speed

For practical wind energy assessment, not all wind speeds are suitable for power generation. Wind turbines have a cut-in speed and a cut-out speed. Therefore, we defined the "Utilizable Wind Speed" as the frequency of occurrence of wind speeds within this

operational range (defined as 3 m/s to 25 m/s in this study). This metric is crucial for estimating the actual operational hours and energy yield of a wind farm [33].

3. Results and Discussion

3.1. Spatiotemporal Patterns of Photovoltaic Power Potential (PVP)

Based on the 30-year climatological assessment results, distinct spatiotemporal patterns in the Photovoltaic Power Potential (PVP) across China's four offshore seas—the Bohai Sea, Yellow Sea, East China Sea, and South China Sea—have been revealed. Spatially, a clear latitudinal gradient is evident. The South China Sea exhibits the highest PVP values throughout the year, with the annual average PVP in its central and northern parts consistently exceeding 16–18%. In contrast, the Bohai, Yellow, and East China Seas generally show lower PVP levels, where the annual average PVP is mainly concentrated between 10 and 14 southern Yellow Sea and the East China Sea display intermediate PVP values, forming a transitional zone between the high-value southern region and the low-value northern region.

All regions show significant seasonal variations (Figures 7 and 8). Solar resources are most abundant during spring and summer (April to August). The South China Sea reaches its peak during this period, with PVP values exceeding 25% across most of its area in months like April. The Bohai Sea, Yellow Sea, and East China Sea also reach their highest PVP during these months, although their absolute values remain lower than those in the southern sea. Conversely, PVP drops to its lowest annual levels during winter (November to February). The decrease is most pronounced in the northern seas, particularly the Bohai Sea and the northern Yellow Sea, where PVP can fall below 12% in December and January. Meanwhile, the South China Sea maintains a relatively high PVP even in winter, with values in its core areas rarely dropping below 14%, highlighting its stability as a solar energy resource.

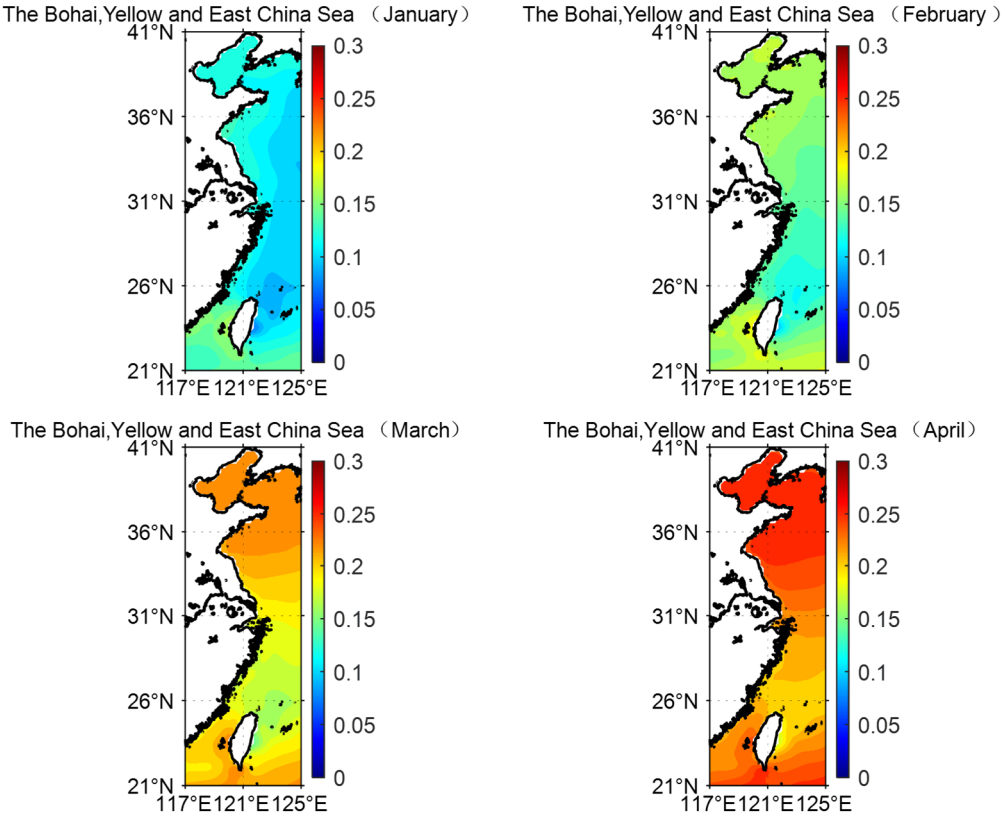


Figure 7. *Cont.*

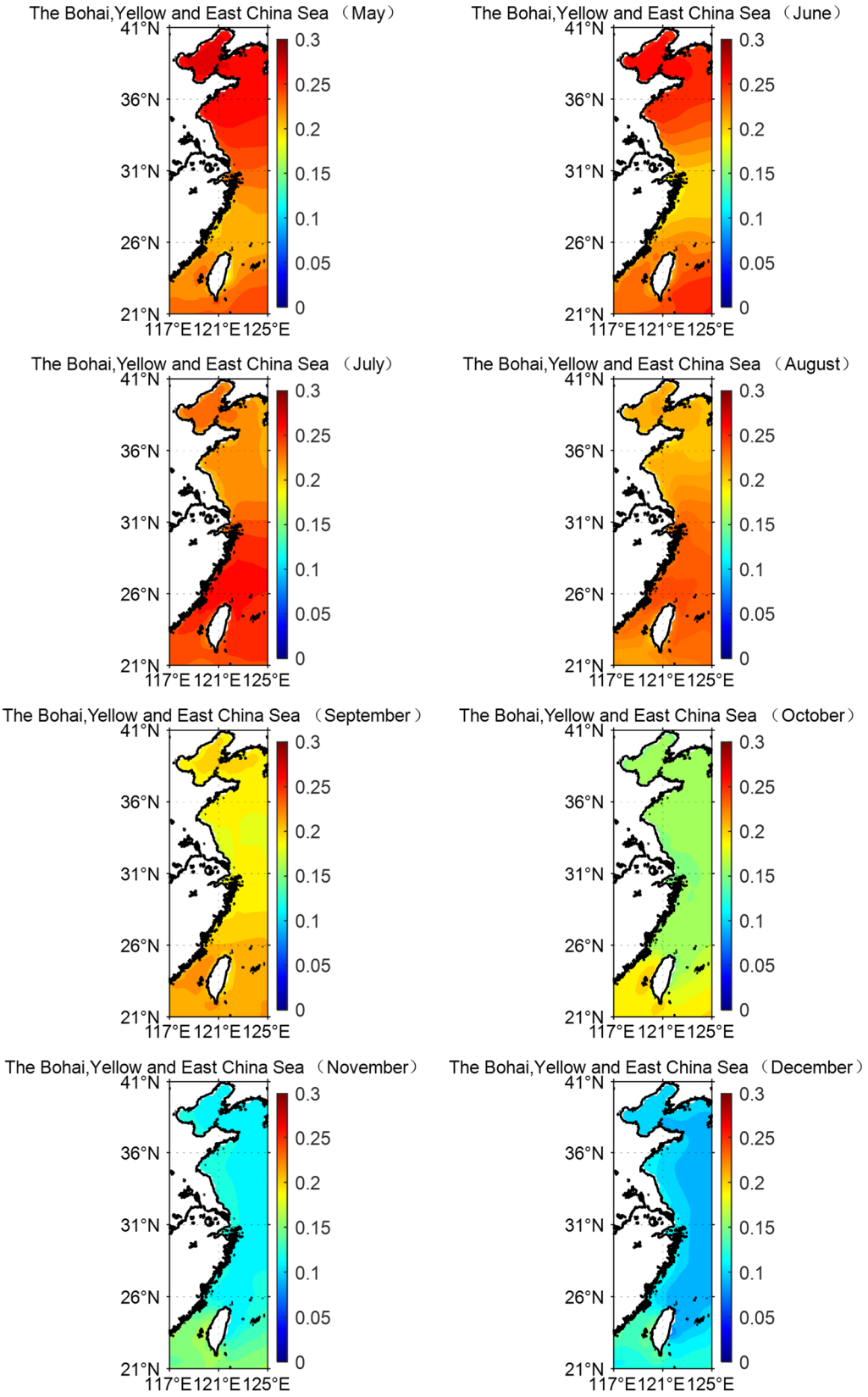


Figure 7. Distribution of Average Photovoltaic Power Potential from January to December (1995–2024) in the Bohai, Yellow, and East China Seas.

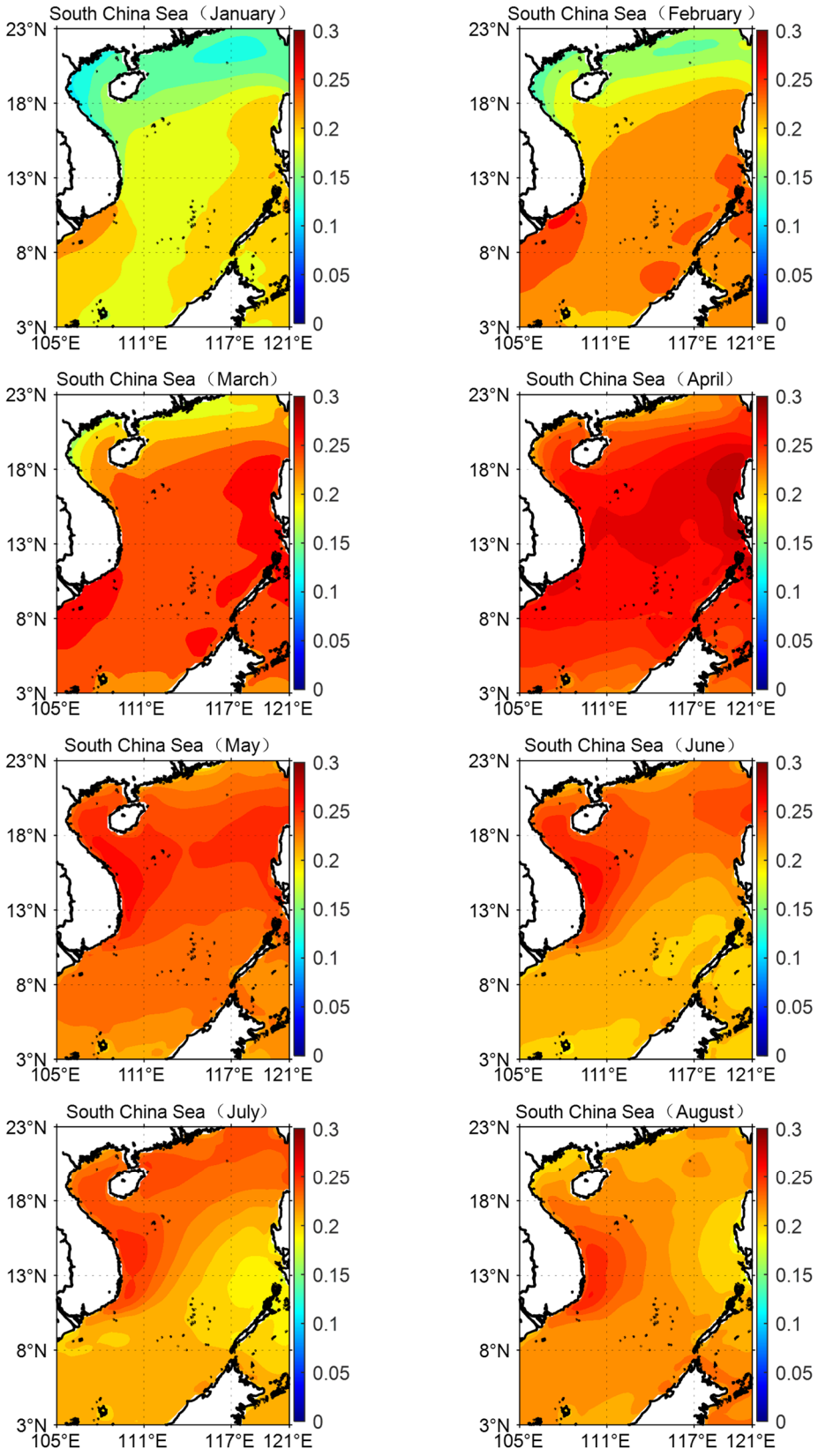


Figure 8. *Cont.*

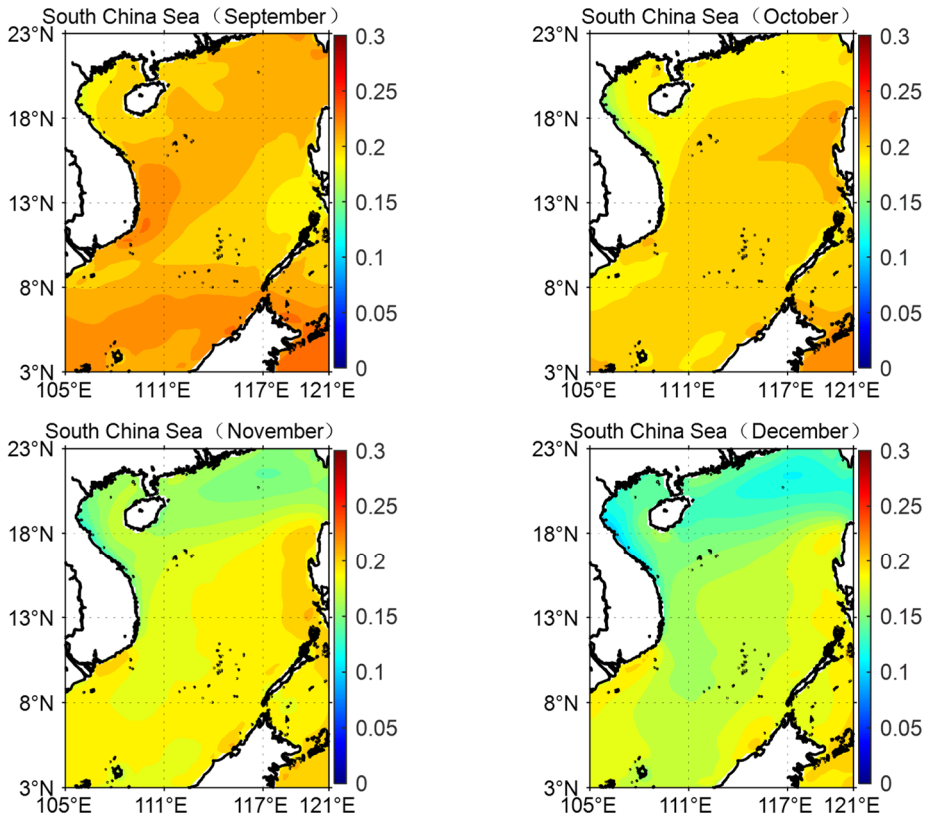


Figure 8. Distribution of Average Photovoltaic Power Potential from January to December (1995–2024) in the South China Sea.

In summary, the spatial distribution of offshore photovoltaic power potential in China shows a decreasing trend from south to north, while the seasonal variation across all seas is characterized by higher values in summer and lower values in winter. The South China Sea stands out as the region with the greatest and most stable potential for offshore solar energy utilization throughout the year.

3.2. Spatial Patterns of Wind Energy Resources

Analysis based on 30-year climate data reveals significant spatial heterogeneity and pronounced seasonal variability in wind energy resources, represented by the wind power density (WPD) at a hub height of 160 m, across China's four offshore seas. Figure 9 shows the annual average frequency of utilizable wind speed (within the 3–25 m/s range) at 10 m height. Overall, the East China Sea, the Taiwan Strait, and the northern South China Sea exhibit the highest frequency of utilizable wind speeds, indicating superior wind resource availability in these regions. In contrast, the frequency is relatively lower over landmasses and in the southern South China Sea.

The spatial distribution of WPD presents a more detailed pattern (Figures 10 and 11). The East China Sea, particularly the Taiwan Strait, is the most energy-rich area year-round, with its annual average WPD in many months far exceeding that of other seas. The northern South China Sea also demonstrates high WPD for most of the year, while the Bohai Sea and the Yellow Sea show relatively weaker overall wind energy potential. The seasonal fluctuation of wind energy resources is highly pronounced. All seas share the common characteristic of being stronger in autumn/winter and weaker in spring/summer. The period of highest WPD is concentrated from October to February. During this time, controlled by the East Asian winter monsoon, the WPD in the East China Sea and the Taiwan Strait often peaks, with monthly averages in some areas exceeding 800–1800 W/m^2.

In stark contrast, summer (June–August) is the low season for wind energy across the entire coastal region, where WPD generally drops to its annual minimum. This is particularly evident in the South China Sea, likely influenced by the transition of summer monsoons and relatively calm conditions before typhoon activity. It is noteworthy that the wind energy distribution in the South China Sea exhibits a unique spatial structure during summer, potentially associated with synoptic weather system activities. Meanwhile, although the Bohai Sea possesses the lowest WPD among the four seas, it still displays a clear seasonal cycle of strong winds in winter and weak winds in summer.

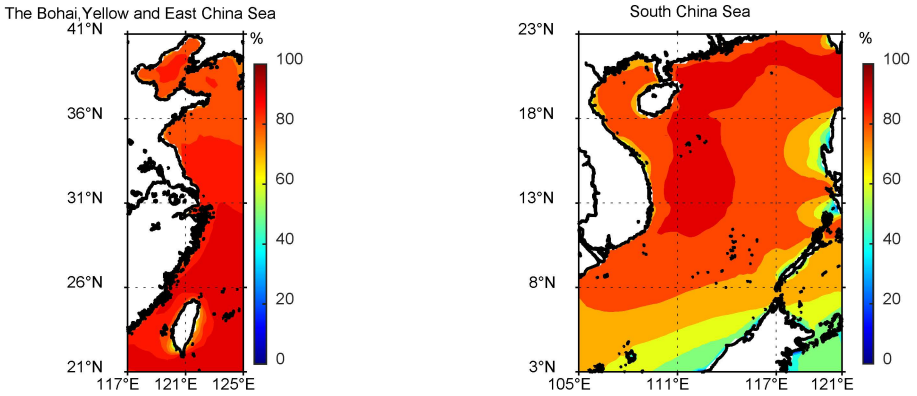


Figure 9. Distribution of Annual Average Available Wind Speed Frequency at 10 m Height in the Bohai Sea, Yellow Sea, East China Sea, and South China Sea (1995–2024).

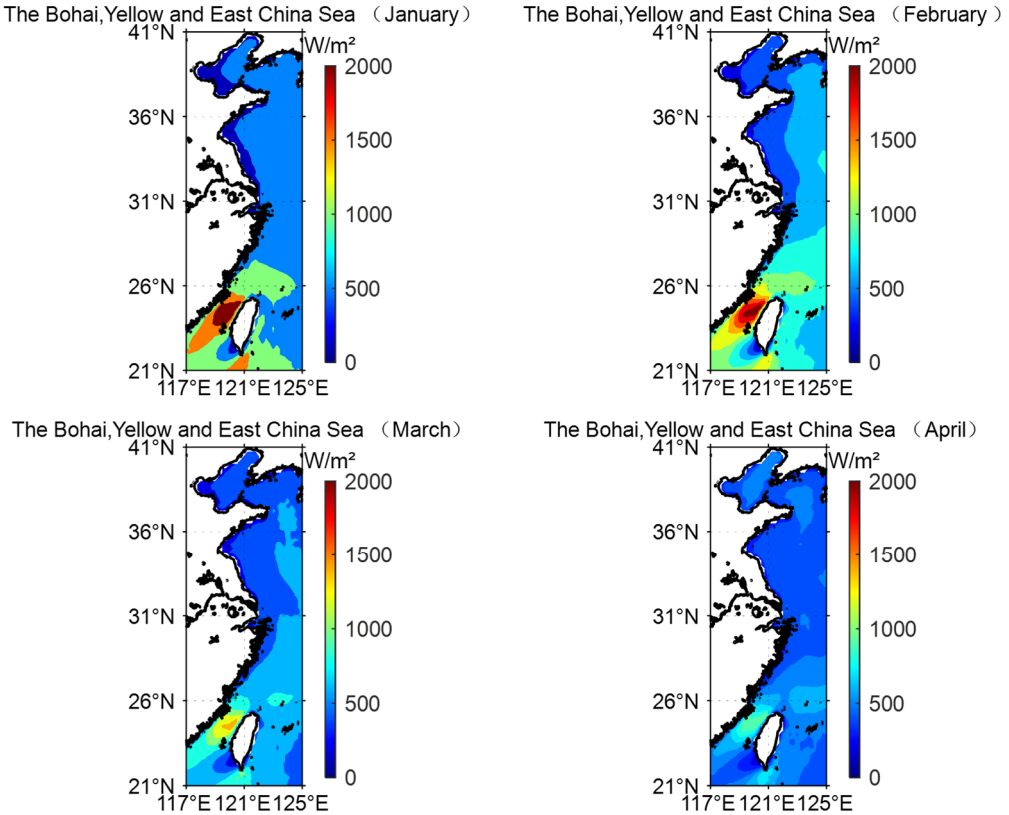


Figure 10. *Cont.*

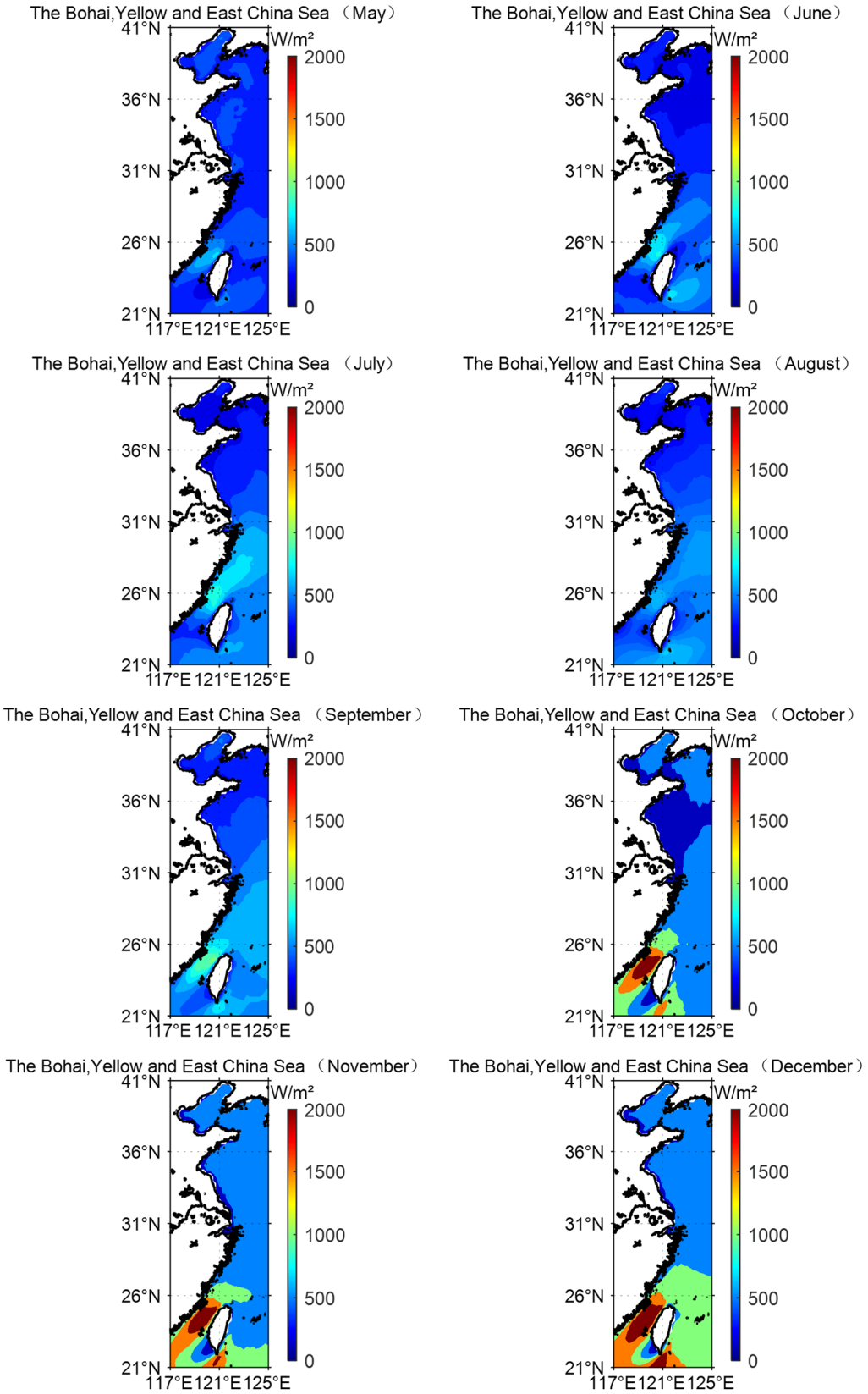


Figure 10. Distribution of Annual Average Available Wind Energy Density at 160 m Height (January–December) in the Bohai Sea, Yellow Sea, and East China Sea (1995–2024).

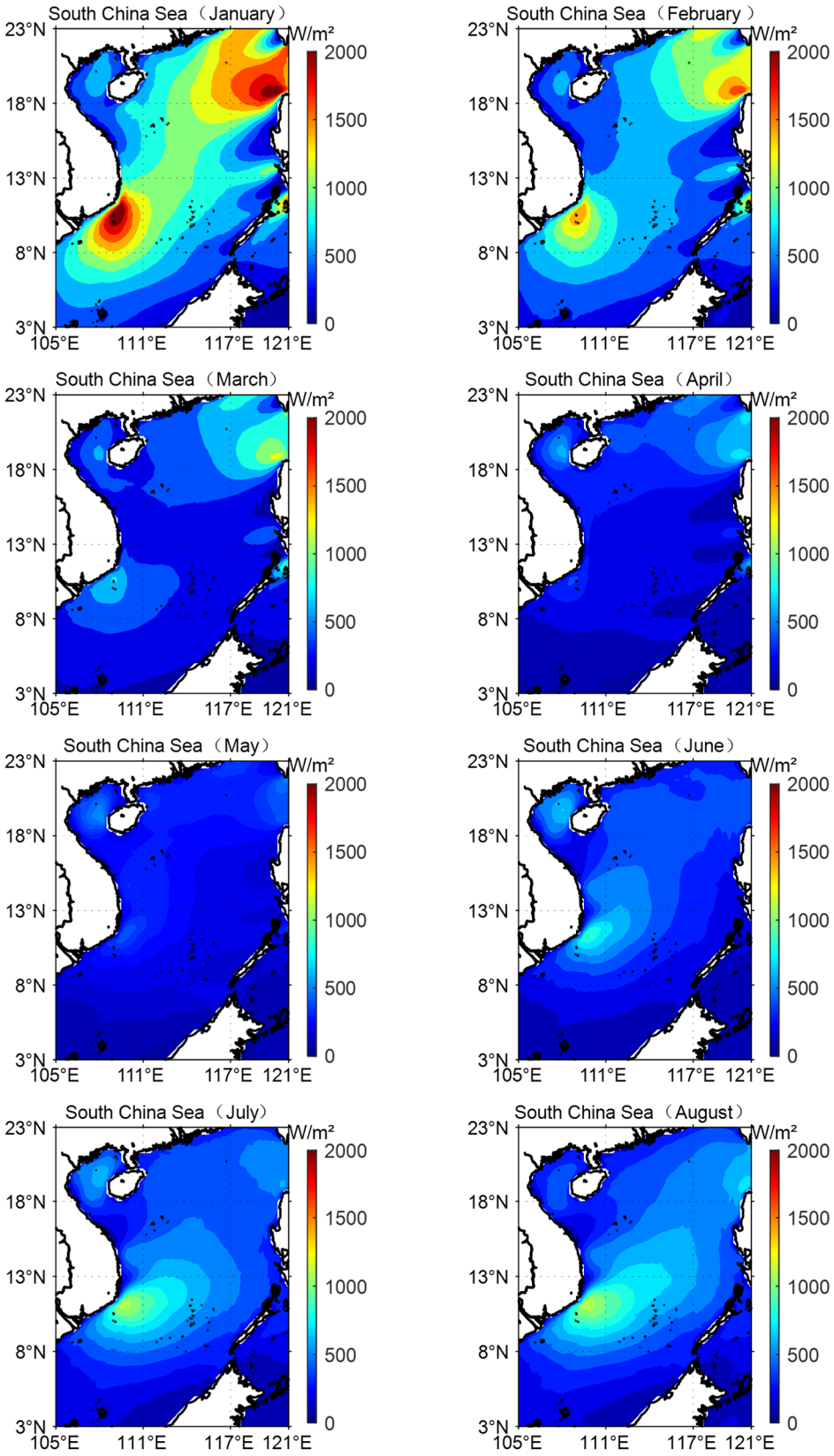


Figure 11. *Cont*.

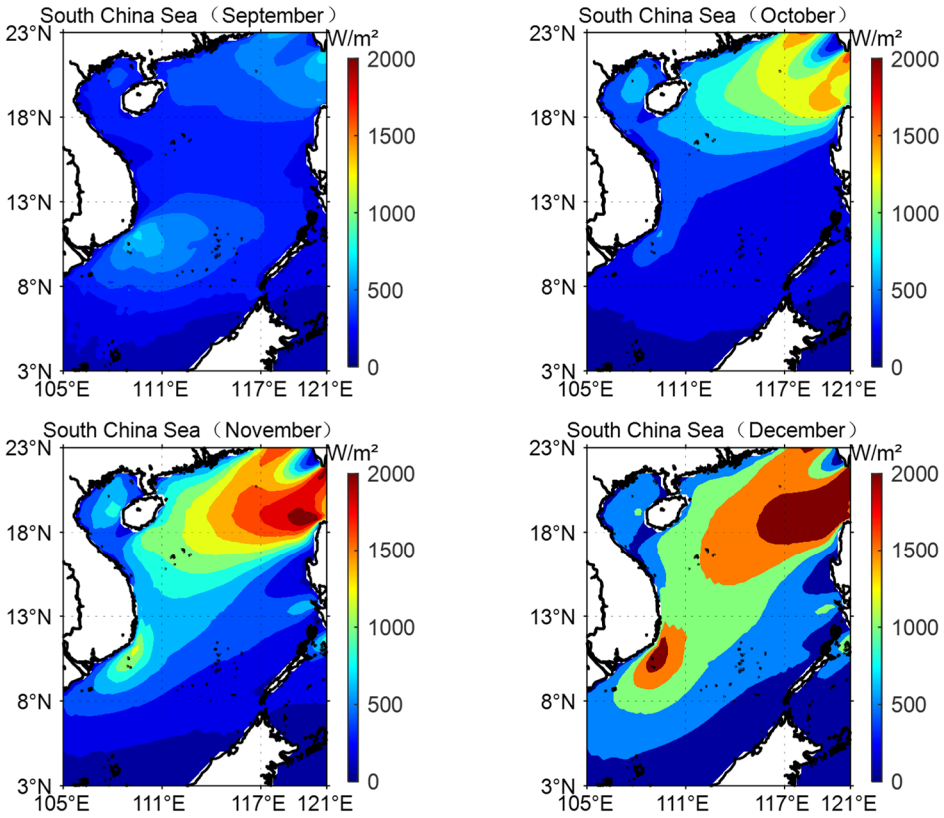


Figure 11. Distribution of Annual Average Available Wind Energy Density at 160 m Height (January–December) in the South China Sea (1995–2024).

In summary, China's offshore wind energy resources are spatially characterized by the East China Sea and the Taiwan Strait as the core high-value zones, and temporally by a highly consistent pattern of abundance in autumn/winter and scarcity in spring/summer.

3.3. Temporal Evolution of Wind and Solar Resources at Representative Coastal Sites

To gain a detailed understanding of the characteristics of wind and solar energy resources along the coastal provinces, a representative site was selected in the offshore area of each of the 11 coastal provinces (from north to south: Liaoning, Tianjin, Hebei, Shandong, Jiangsu, Shanghai, Zhejiang, Fujian, Guangdong, Guangxi, and Hainan) (Figure 12). The geographical coordinates of these sites are provided in Table 4. The monthly time series of Photovoltaic Power Potential (PVP) and Wind Power Density (E) at these sites from 1995 to 2024 were analyzed (Figures 13 and 14).

Table 4. Latitude and Longitude of Selected Points in Coastal Provinces.

Station (Water Depth)	Longitude (°E)	Latitude (°N)
Liaoning (10 m)	121.135	39.085
Tianjin (10 m)	118.006	38.765
Hebei (10 m)	119.71	39.51
Shandong (50 m)	122.61	36.252
Jiangsu (50 m)	121.894	34.552
Shanghai (50 m)	122.723	31.335
Zhejiang (50 m)	122.585	29.069
Fujian (50 m)	120.144	25.198

Table 4. *Cont.*

Station (Water Depth)	Longitude (°E)	Latitude (°N)
Guangdong (50 m)	112.644	21.219
Guangxi (50 m)	108.44	20.577
Hainan (50 m)	110.506	18.681

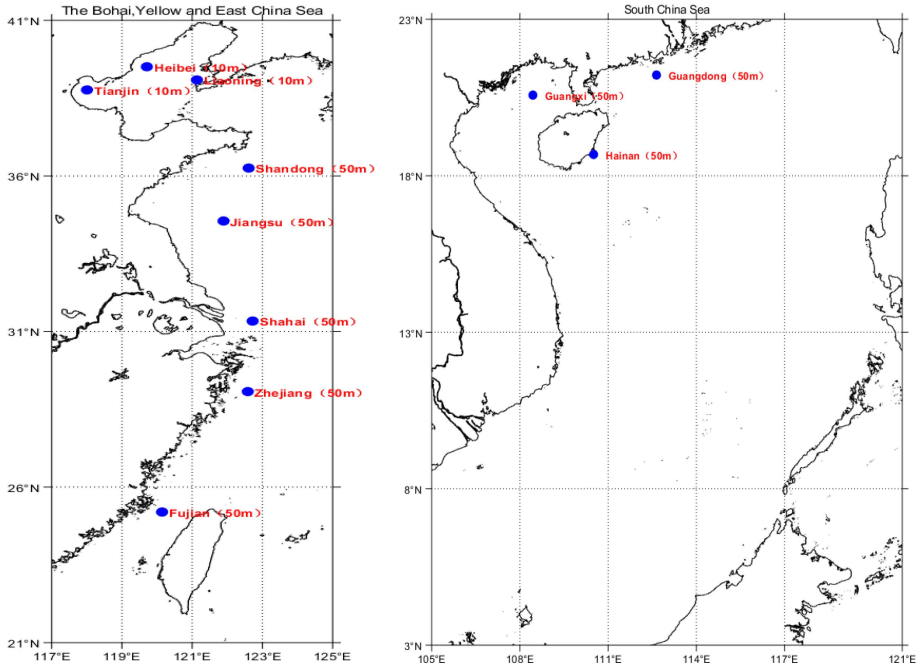


Figure 12. Distribution Map of Selected Points in Coastal Provinces.

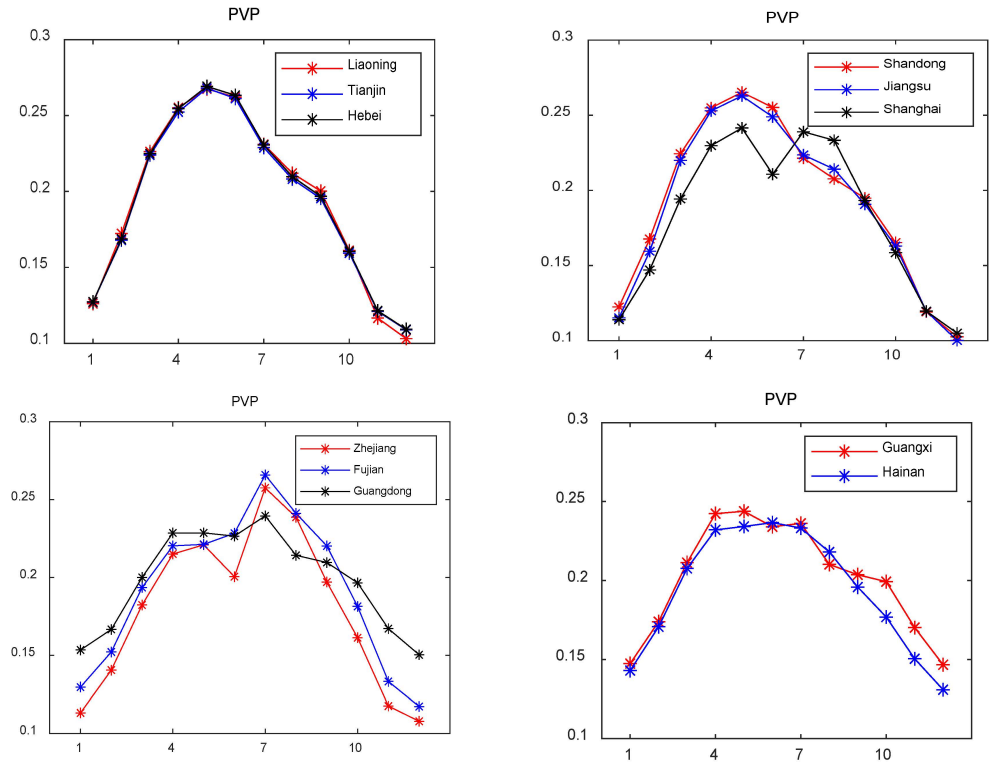


Figure 13. Time Series Diagram of Photovoltaic Power Generation Potential at Selected Locations in Coastal Provinces.

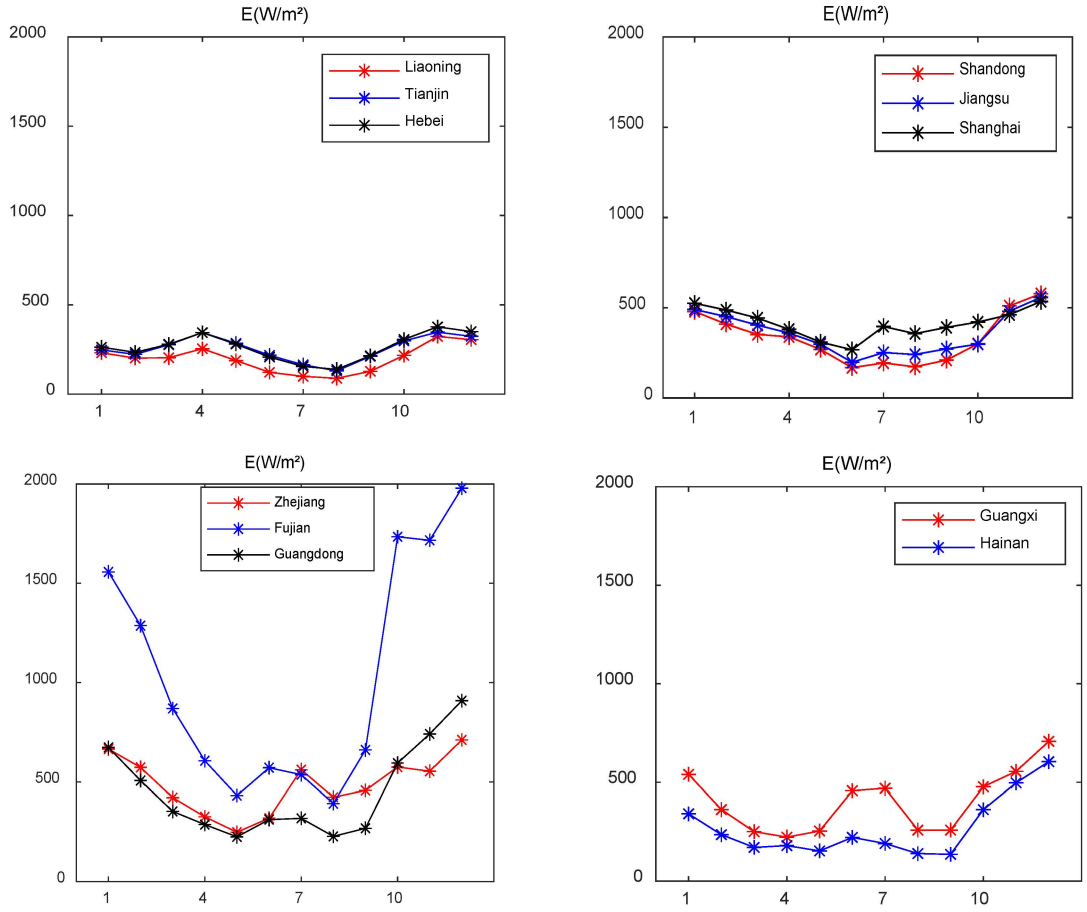


Figure 14. Time Series Diagram of Wind Energy at Selected Locations in Coastal Provinces.

The Photovoltaic Power Potential (PVP) at all sites exhibited a stable, annual cyclical pattern. PVP peaks consistently occurred during spring and summer (April–August), while troughs were concentrated in autumn and winter (November–February). The amplitude of this seasonal oscillation showed pronounced latitudinal variation: northern sites (e.g., Liaoning, Hebei) experienced the most dramatic seasonal differences in PVP, with a sharp contrast between summer peaks and winter lows. In contrast, southern sites (e.g., Guangxi, Hainan) maintained relatively high PVP levels throughout the year with milder seasonal fluctuations, indicating more stable power generation potential.

The temporal evolution of Wind Power Density (E) exhibited a phase almost opposite to that of PVP. Wind resources at all sites were most abundant during autumn and winter (October to February) and reached their annual minimum during spring and summer (May–August). Among all sites, the selected site in Fujian exhibited the strongest wind power density and the most pronounced seasonal variability during winter, far exceeding levels observed in other regions. In comparison, sites along the Bohai Sea (e.g., Tianjin, Hebei) showed lower overall wind power density levels but still followed the common pattern of stronger winds in winter and weaker winds in summer.

Overall, the time series from these representative sites clearly demonstrate a natural complementary characteristic between wind energy (strong in autumn/winter) and solar energy (strong in spring/summer) along China's coast. This complementary relationship is most evident on a seasonal scale, providing favorable natural conditions for constructing integrated wind–solar hybrid power systems and mitigating fluctuations in total power output.

4. Conclusions

Based on the ERA5 reanalysis dataset, this study conducted a comprehensive 30-year (1995–2024) spatiotemporal assessment of wind and photovoltaic power potential across China's four major offshore seas: the Bohai Sea, Yellow Sea, East China Sea, and South China Sea. By systematically analyzing monthly spatial patterns, temporal evolution at representative sites, and wind regime characteristics, the following main conclusions are drawn:

Photovoltaic Power Potential (PVP) exhibits a distinct latitudinal gradient and seasonal variability. The South China Sea shows the highest annual PVP (16–18%), with summer peaks exceeding 25%, while the Bohai and Yellow Seas have lower PVP, dropping below 12% in winter. Overall, solar resources decrease from south to north and are higher in summer and lower in winter. Wind energy resources show strong spatial heterogeneity, with the East China Sea and Taiwan Strait as the core high-value zones. The annual average wind power density in these regions often exceeds 800–1800 W/m^2 during autumn and winter, significantly outperforming other seas. Wind resources consistently follow a monsoon-influenced pattern of being stronger in autumn/winter and weaker in spring/summer. A clear temporal complementarity exists between wind and solar resources. Time series analyses at all representative coastal sites reveal that wind power peaks in autumn/winter, while solar power peaks in spring/summer. This natural complementary pattern offers favorable conditions for developing integrated wind–solar hybrid power systems. The South China Sea stands out for its stable and high solar potential, whereas the East China Sea leads in wind energy intensity and utilizable frequency. The South China Sea is suitable for large-scale offshore PV deployment, while the East China Sea is ideal for concentrated offshore wind development. The distinct resource endowments of different sea areas support regionally differentiated energy planning.

This study fills a critical gap in the long-term systematic assessment of offshore wind and solar resources in China. It provides data support and theoretical insights for renewable energy planning, optimal siting of wind turbines and PV arrays, and the design of hybrid energy systems in coastal provinces. Future work should integrate marine environmental constraints, techno-economic analysis, and grid integration capabilities to facilitate the efficient development and utilization of China's offshore renewable energy.

Author Contributions: Conceptualization, Y.W. and Y.B.; methodology, H.W.; software, Y.W.; validation, Y.W., Y.B. and Q.Z.; formal analysis, Y.W.; investigation, Q.Z.; resources, H.W.; data curation, Y.B.; writing—original draft preparation, Y.W.; writing—review and editing, H.W.; visualization, Y.W.; supervision, Q.Z.; project administration, Y.W.; funding acquisition, H.W. All authors have read and agreed to the published version of the manuscript.

Funding: This study was financially supported by the National Key Research and Development Program of China (2023YFC3106901).

Data Availability Statement: The original contributions presented in this study are included in the article. Further inquiries can be directed to the corresponding author.

Conflicts of Interest: The authors declare no conflict of interest.

References

1. Hassan, Q.; Viktor, P.; Al-Musawi, T.J.; Ali, B.M.; Algburi, S.; Alzoubi, H.M.; Al-Jiboory, A.K.; Sameen, A.Z.; Salman, H.M.; Jaszczur, M. The renewable energy role in the global energy Transformations. *Renew. Energy Focus* **2024**, *48*, 100545. [CrossRef]
2. Saleh, H.M.; Hassan, A.I. The challenges of sustainable energy transition: A focus on renewable energy. *Appl. Chem. Eng.* **2024**, *7*, 2084. [CrossRef]
3. Gielen, D.; Boshell, F.; Saygin, D.; Bazilian, M.D.; Wagner, N.; Gorini, R. The role of renewable energy in the global energy transformation. *Energy Strategy Rev.* **2019**, *24*, 38–50. [CrossRef]

4. Zhang, X.; Zhong, J.; Zhang, X.; Zhang, D.; Miao, C.; Wang, D.; Guo, L. China can achieve carbon neutrality in line with the Paris Agreement's 2 C target: Navigating global emissions scenarios, warming levels, and extreme event projections. *Engineering* **2025**, *44*, 207–214. [CrossRef]
5. Obane, H.; Nagai, Y.; Asano, K. Assessing land use and potential conflict in solar and onshore wind energy in Japan. *Renew. Energy* **2020**, *160*, 842–851. [CrossRef]
6. Richardson, J.; Kirk Hall, P.; Morgan, W. Land Use Conflicts Between Wind and Solar Renewable Energy and Agricultural Uses. Ph.D. Thesis, West Virginia University, Morgantown, WV, USA, 2022.
7. Wen, Y.; Lin, P. Offshore solar photovoltaic potential in the seas around China. *Appl. Energy* **2024**, *376*, 124279. [CrossRef]
8. Weiss, C.V.; Guanche, R.; Ondiviela, B.; Castellanos, O.F.; Juanes, J. Marine renewable energy potential: A global perspective for offshore wind and wave exploitation. *Energy Convers. Manag.* **2018**, *177*, 43–54. [CrossRef]
9. Li, J.; Wang, G.; Li, Z.; Yang, S.; Chong, W.T.; Xiang, X. A review on development of offshore wind energy conversion system. *Int. J. Energy Res.* **2020**, *44*, 9283–9297. [CrossRef]
10. Yuan, X.-C.; Lyu, Y.-J.; Wang, B.; Liu, Q.-H.; Wu, Q. China's energy transition strategy at the city level: The role of renewable energy. *J. Clean. Prod.* **2018**, *205*, 980–986. [CrossRef]
11. Li, P.; Lian, J.; Ma, C.; Zhang, J. Complementarity and development potential assessment of offshore wind and solar resources in China seas. *Energy Convers. Manag.* **2023**, *296*, 117705. [CrossRef]
12. Tian, J.; Zhou, S.; Wang, Y. Assessing the technical and economic potential of wind and solar energy in China—A provincial-scale analysis. *Environ. Impact Assess. Rev.* **2023**, *102*, 107161. [CrossRef]
13. Jiang, H.; Yao, L.; Zhou, C. Assessment of offshore wind-solar energy potentials and spatial layout optimization in mainland China. *Ocean Eng.* **2023**, *287*, 115914. [CrossRef]
14. Wang, Y.; Chao, Q.; Zhao, L.; Chang, R. Assessment of wind and photovoltaic power potential in China. *Carbon Neutrality* **2022**, *11*, 15. [CrossRef]
15. Zheng, C.W.; Li, C.Y.; Pan, J.; Liu, M.Y.; Xia, L.L. An overview of global ocean wind energy resource evaluations. *Renew. Sustain. Energy Rev.* **2016**, *53*, 1240–1251. [CrossRef]
16. Wang, X.H.; Cho, Y.-K.; Guo, X.; Wu, C.-R.; Zhou, J. The status of coastal oceanography in heavily impacted Yellow and East China Sea: Past trends, progress, and possible futures. *Estuar. Coast. Shelf Sci.* **2015**, *163*, 235–243. [CrossRef]
17. Chen, C.-T.A. Chemical and physical fronts in the Bohai, Yellow and East China seas. *J. Mar. Syst.* **2009**, *78*, 394–410. [CrossRef]
18. Schindler, D.; Behr, H.D.; Jung, C. On the spatiotemporal variability and potential of complementarity of wind and solar resources. *Energy Convers. Manag.* **2020**, *218*, 113016. [CrossRef]
19. Graabak, I.; Korpås, M. Variability characteristics of European wind and solar power resources—A review. *Energies* **2016**, *9*, 449. [CrossRef]
20. Das, P.; Mathur, J.; Bhakar, R.; Kanudia, A. Implications of short-term renewable energy resource intermittency in long-term power system planning. *Energy Strategy Rev.* **2018**, *22*, 1–15. [CrossRef]
21. Emmanuel, M.; Doubleday, K.; Cakir, B.; Marković, M.; Hodge, B.-M. A review of power system planning and operational models for flexibility assessment in high solar energy penetration scenarios. *Sol. Energy* **2020**, *210*, 169–180. [CrossRef]
22. Hersbach, H.; Bell, B.; Berrisford, P.; Hirahara, S.; Horányi, A.; Muñoz-Sabater, J.; Nicolas, J.; Peubey, C.; Radu, R.; Schepers, D.; et al. The ERA5 global reanalysis. *Q. J. R. Meteorol. Soc.* **2020**, *146*, 1999–2049. [CrossRef]
23. Hersbach, H. The ERA5 atmospheric reanalysis. In *AGU Fall Meeting Abstracts*; American Geophysical Union: Washington, DC, USA, 2016; p. NG33D-01.
24. Chan, J.C.L.; Williams, R.T. Analytical and Numerical Studies of the Beta-Effect in Tropical Cyclone Motion. Part I: Zero Mean Flow. *J. Atmos. Sci.* **1987**, *44*, 1257–1265. [CrossRef]
25. Zheng, C.-W.; Pan, J.; Li, J.-X. Assessing the China Sea wind energy and wave energy resources from 1988 to 2009. *Ocean Eng.* **2013**, *65*, 39–48. [CrossRef]
26. He, J.; Yang, K.; Tang, W.; Lu, H.; Qin, J.; Chen, Y.; Li, X. The first high-resolution meteorological forcing dataset for land process studies over China. *Sci. Data* **2020**, *7*, 25. [CrossRef]
27. Jerez, S.; Tobin, I.; Vautard, R.; Montávez, J.P.; López-Romero, J.M.; Thais, F.; Bartok, B.; Christensen, O.B.; Colette, A.; Déqué, M.; et al. The impact of climate change on photovoltaic power generation in Europe. *Nat. Commun.* **2015**, *6*, 10014. [CrossRef]
28. Mavromatakis, F.; Makrides, G.; Georghiou, G.; Pothrakis, A.; Franghiadakis, Y.; Drakakis, E.; Koudoumas, E. Modeling the photovoltaic potential of a site. *Renew. Energy* **2010**, *35*, 1387–1390. [CrossRef]
29. Chenni, R.; Makhlouf, M.; Kerbache, T.; Bouzid, A. A detailed modeling method for photovoltaic cells. *Energy* **2007**, *32*, 1724–1730. [CrossRef]
30. Kozai, K.; Ohsawa, T.; Takahashi, R.; Takeyama, Y. Evaluation method for offshore wind energy resources using scatterometer and Weibull parameters. *J. Energy Power Eng.* **2012**, *6*, 1772.

31. Hasager, C.B.; Mouche, A.; Badger, M.; Bingöl, F.; Karagali, I.; Driesenaar, T.; Stoffelen, A.; Peña, A.; Longépé, N. Offshore wind climatology based on synergetic use of Envisat ASAR, ASCAT and QuikSCAT. *Remote Sens. Environ.* **2015**, *156*, 247–263. [CrossRef]
32. Yu, S.; Vautard, R. A transfer method to estimate hub-height wind speed from 10 meters wind speed based on machine learning. *Renew. Sustain. Energy Rev.* **2022**, *169*, 112897. [CrossRef]
33. Moghaddam, S.Z. Generation and transmission expansion planning with high penetration of wind farms considering spatial distribution of wind speed. *Int. J. Electr. Power Energy Syst.* **2019**, *106*, 232–241. [CrossRef]

Disclaimer/Publisher's Note: The statements, opinions and data contained in all publications are solely those of the individual author(s) and contributor(s) and not of MDPI and/or the editor(s). MDPI and/or the editor(s) disclaim responsibility for any injury to people or property resulting from any ideas, methods, instructions or products referred to in the content.